Journal of Applied Fluid Mechanics, Vol. 17, No. 9, pp. 1896-1911, 2024.
Available online at www.jafmonline.net, ISSN 1735-3572, EISSN 1735-3645.
https://doi.org/10.47176/jafm.17.9.2525

A Numerical Study on Effects of Ice Formation on Vertical-axis Wind Turbine Performance and Flow Field at Optimal Tip Speed Ratio

S. Abbasi[1†], A. Mahmoodi[1] and A. Joodaki[2]

[1] *Department of Mechanical Engineering, Arak University of Technology, Arak, Iran*
[2] *Faculty of Engineering, University of Ayatollah Alozma Boroujerdi, Boroujerd, Iran*

†Corresponding Author Email: s_abbasi@arakut.ac.ir

ABSTRACT

Wind turbines can freeze due to exposure to cold air. Ice formation on the rotor blades of a wind turbine reduces their performance. In the present work, the effects of ice formation on rotor blades of straight-blade vertical-axis wind turbines (SBVAWT) with a three-blade rotor and a NACA 0021 airfoil are numerically evaluated under two-dimensional transient settings by solving the continuity, momentum and turbulence equations become in ANSYS FLUENT. Grid and time step independence was investigated. For validation, the numerical model was compared with experimental data. An experimental ice model from the literature was then used to numerically simulate the iced rotor in two-dimensional transition settings. The numerical simulation of the icy rotor was compared with an ice-free rotor. It was found that ice formation on the rotor blades changed the velocity and pressure fields around the rotor blades at angles of 180—360°, changing the streamlines and increasing the vortices. Furthermore, the maximum and minimum reductions in moment coefficient during blade icing occurred at angles of 225—315° and 45—135°, respectively. Due to ice formation on the rotor blades, the power coefficient of the rotor blades at angles 180—360° decreased drastically, and the power coefficient of the iced rotor was smaller than that of an ice-free rotor. It was concluded that ice formation on the blades of the SBVAWT reduced the average power coefficient of the blades and rotor power coefficient by 94.2% and 95%, respectively.

Article History

Received December 19, 2023
Revised March 17, 2024
Accepted April 8, 2024
Available online July 2, 2024

Keywords:

Wind turbine
Vertical axis
Straight blade
Increased icing
Performance

1. INTRODUCTION

With population growth in recent years, the need for energy has also increased. Although fossil fuels are still the most widespread and readily available energy sources, they cannot meet all of the energy needs of people on the planet because they are not evenly distributed around the world. Wind energy is one of the renewable energy sources that is gaining attention due to its availability in other parts of the world and its cost-effectiveness. Cold regions have the advantages of high wind speed and low population. In these areas, wind turbines are typically exposed to freezing conditions, which adversely affects their performance. The formation of ice on the rotor blades of wind turbines by changing the aerodynamic properties of the rotor blades leads to undesirable power losses. It also shortens the service life of wind turbine components (Sagol, 2014 Yirtici et al., 2019).

Wind turbines are divided into the general category of horizontal axis wind turbines and vertical axis wind turbines. In horizontal wind turbines, depending on the internal structure and operation mode, ice accumulates on the leading edge of the rotor blades (Jin & Virk, 2020a Wang et al., 2020 Gao & Hu, 2021). The ice formed on the leading edge of the blade changes the blade pressure coefficient (Ebrahimi et al., 2016 Hu et al., 2018 Shu et al., 2018a Son & Kim, 2020). A change in the pressure coefficient due to the change in the flow field around the blade changes the aerodynamic coefficients of the blade. In this state, the buoyancy force coefficient decreases and the drag force coefficient increases (Hu et al., 2017 Ibrahim et al., 2018). A reduction in the aerodynamic coefficients of the rotor blades leads to a reduction in the output power of a horizontal axis wind turbine (Lamraoui et al., 2014 Imran et al., 2016 Shu et al., 2017 Shu et al., 2018b Zhu et al., 2018 Gao & Hong, 2021 Gao et al., 2021Yirtici & Tuncer, 2021). For horizontal-axis wind turbines, some studies have addressed

Nomenclature

c	chord line	F_D	drag force
H	blade height	C_D	drag force coefficient
R	rotor radius	F_T	tangential force
A	wind turbine area	C_T	tangential force coefficient
θ	Azimuth angle	F_N	radial force
α	angle of attack	C_N	radial force coefficient
β	pitch angle	M	moment
φ	the sum of the angle of attack and pitch angle	C_m	moment coefficient
ρ	density	P	power
μ	dynamic viscosity	C_P	power coefficient
ν	kinematic viscosity	HAWT	Horizontal Axis Wind Turbine
T_∞	temperature	SBVAWT	Straight Blade Vertical Axis Wind Turbine
V_∞	wind speed	TSR	Tip Speed Ratio
ω	angular velocity	LWC	Liquide Water Content
V_{rel}	relative velocity	MVD	Median Volume Droplet Diameter
V_t	tangential velocity	SMT	Sliding Mesh Technique
V_n	radial velocity	MRF	Multiple Reference Frame
t	time	2d	two dimensional
F_L	lift force	CW	clockwise
C_L	lift force coefficient	CCW	counterclockwise

the shape and amount of ice as well as its influencing factors and ice simulation methods (Zhu et al., 2015 Li et al., 2018b Kreutz et al., 2019 Li et al., 2019a, b; Jin & Virk, 2020b, Shi et al., 2021 Son et al., 2021). Due to the abundance of horizontal axis wind turbines, many studies have been conducted on them, but not many studies have been conducted on ice in vertical axis wind turbines.

Vertical axis wind turbines differ fundamentally from horizontal axis wind turbines in their design and operation. For this reason, the shape and location of ice accumulation in them is very different from horizontal axis wind turbines. The angle of attack of the wings is the main factor in determining the location of ice accumulation. With statically symmetrical airfoils, ice accumulates on the leading edge. However, in asymmetric airfoils, vortices arise near the trailing edge due to the curvature of the chord line, which leads to the formation of ice on the trailing edge of the blade (Li et al., 2014, 2015 Manatbayev et al., 2021).

With rotating rotors, the shape and location of ice formation on the rotor blades are completely different. In general, objects rotating in a plane parallel to the Earth's surface experience different angles of attack depending on the direction of the wind during one revolution around the center of the rotor. On the other hand, the level of the peak speed ratio, which results from dividing the tangential speed by the wind speed, influences the determination of the angle of attack. Therefore, the shape and location of ice formation on objects rotating in a plane parallel to the Earth's surface largely depends on the angle of attack. On the other hand, research shows that the amount of ice depends on the duration of freezing (Li et al., 2020 Guo et al., 2021b). For wind turbines with straight blades and a vertical axis, increasing the freezing time and average liquid volume increases the ice mass that forms on the blades. Additionally, the amount of ice accumulated increases as the number of blades increases. Because of the greater fluctuations in flow, a three-blade rotor will accumulate more ice than a two-blade rotor. The peak velocity ratio parameter affects the nonuniformity of ice thickness. At peak velocity ratios below unity, the flow and angular velocity of the blade allow the water droplets to settle over the entire surface of the blade and a layer of ice to cover the entire surface of the blade. Although at peak speed ratios close to one the ice thickness increases slightly near the leading and trailing edges, at speed ratios below one the ice thickness can be said to be almost the same everywhere on the blade. At higher speed ratios, the thickness of the ice changes with the blade rotation direction, and at very high speed ratios, the ice cannot cover the entire surface of the blade (Li et al., 2018a Baizhuma et al., 2021 Guo et al., 2021a). The research carried out shows that the formation of ice rime frost on the rotor blades of the direct blade vertical axis wind turbine reduces the output power, but the wind turbine can still produce positive power. However, due to the formation of glaze ice on the rotor blades, the wind turbine is no longer able to generate positive power and is completely excluded from the power generation cycle. In general, the formation of ice on the blades of a wind turbine with straight blades and a vertical axis leads to violent flow fluctuations. Fluctuations are caused by a change in the shape of the blades and a roughening of their surface. In this case, the lift coefficient of frozen rotor blades decreases and their drag coefficient increases. In this condition, the torque coefficient and power of the blades are significantly reduced, and the average power of the rotor is reduced by 80% (Li et al., 2010 Baizhuma et al., 2021 Manatbayev et al., 2021).

When discussing wind turbines, it is important to check the flow around the blades. Stability calculations of boundary layer profiles for the Joukowski airfoil show

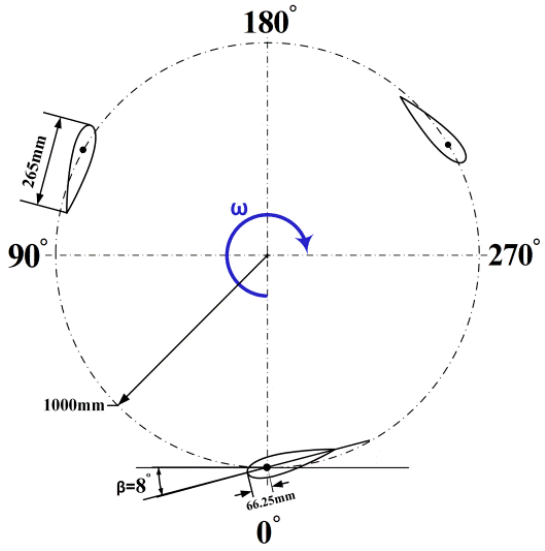

Fig. 1 2D view of the SBVAWT and numerical model dimensions

no branching points that would lead to absolute instability ahead of the trailing edge. However, behind the trailing edge, separation plays a crucial role in increasing the area of absolute instability as the wing thickness increases (Turkyılmazoglu, 1999). Studying the phenomenon of absolute instability of airfoils can help with this topic. The separation phenomenon arises from a sufficiently unfavorable pressure gradient in the boundary layer interaction region with an increase in the wing thickness or the flow viscosity. A strong unfavorable pressure gradient at the boundary layer in front of the separation point forces a subsonic separation. This in turn leads to the mean flow profiles in the interaction area assuming bending shapes that clearly reach the state of absolute instability. The separation contribution to the occurrence of such instability is significantly increased due to the thickening of the airfoil through the interaction process near the trailing edge region. Finally, the pronounced instability caused by the above processes will certainly lead to an unlimited growth of internal disturbances, as a result of which the smooth-turbulent transition will inevitably proceed (Turkyılmazoglu, 2002a). Flow separation near the trailing edge of the airfoil should be investigated. If the angle of attack is small or disappears, the flow will stick over the wing shape and the separation will inevitably occur exactly at the trailing edge. However, if the angle of attack is sufficiently large, the separation must first occur near the leading edge of the wing, resulting in short or long separation bubbles. These separated zones, in turn, promote the laminar flow from the laminar state to the turbulent state (Turkyılmazoglu, 2002b).

Apparently, little research has been done into ice formation and its effects on straight-blade, vertical-axis wind turbines. The few studies that have been carried out in this area focus on the simulation of ice, and the effects of ice on the performance of wind turbines and the factors affecting them have not been studied in detail. Given the diverse complexity of the flow in direct blade, vertical axis wind turbines, the phenomenon of freezing in them is expected to be further investigated. On the other hand, it has been found that the formation of ice on the blades of a wind turbine with straight blades and a vertical axis has a very destructive effect on its performance. Therefore, it is necessary to study this phenomenon in more detail so that the results obtained are useful in determining and designing ice control solutions. Few researchers have studied the ice phenomenon on a two-blade rotor, and this phenomenon has not yet been studied on a three-blade rotor. Since the flow fluctuations are stronger in three-bladed rotors, the effects of ice formation on the performance and flow fluctuations of a three-bladed rotor are discussed in detail in the present study.

2. NUMERICAL SIMULATION OF THE ICE-FREE ROTOR

2.1 Governing Equations

The flow was assumed to be incompressible. The continuity equation is defined as:

$$\frac{\partial \rho}{\partial t} + \nabla.(\rho u) = 0 \tag{1}$$

where ρ is the density while u(x,t) denotes the velocity. The momentum equation is given by:

$$\frac{\partial u}{\partial t} + u.\nabla u - \nu \Delta u = -\frac{1}{\rho}\nabla P + g \tag{2}$$

Here ν is the kinematic viscosity, P(x,t) is the pressure and g(x,t) is the acceleration per unit mass. The flow was assumed to be turbulent and the kω SST turbulence model was used. Here k, ω and eddy viscosity are written as follows:

$$\rho\frac{\partial k}{\partial t} + \rho U_j\frac{\partial k}{\partial x_j} = \frac{\partial}{\partial x_j}\left[(\mu + \sigma_k\mu_t)\frac{\partial k}{\partial x_j}\right] + \tau_{ij}\frac{\partial U_i}{\partial x_j} - \beta^*\rho k\omega \tag{3}$$

$$\rho\frac{\partial \omega}{\partial t} + \rho U_j\frac{\partial \omega}{\partial x_j} = \frac{\partial}{\partial x_j}\left[(\mu + \sigma_\omega\mu_t)\frac{\partial \omega}{\partial x_j}\right] + \alpha\frac{\omega}{k}\tau_{ij}\frac{\partial U_i}{\partial x_j} - \beta^*\rho k\omega^2 \tag{4}$$

$$\mu_t = \frac{\rho k}{\omega} \tag{5}$$

Where the empirical coefficients are given by:

$$\sigma_k = \frac{1}{2}, \sigma_\omega = \frac{1}{2}, \beta^* = \frac{9}{100}, \beta = \frac{3}{40}, \alpha = \frac{5}{9}$$

2.2 SBVAWT Geometry

The 2D view of the SVAWT is shown in Fig. 1. The experimental three-bladed SBVAWT model of An (Maeda et al., 2015) with a rotor radius of 1000 mm and a height of 1200 mm was numerically simulated in 2D settings. The rotor blades had a NACA 0021 airfoil with a chord line of 265 mm. The chord line of the airfoil had an 8° counterclockwise (CCW) rotation about a point 66.25 mm from the leading edge.

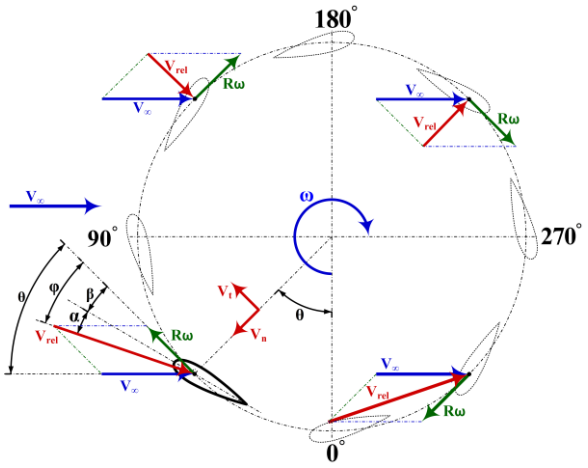

Fig. 2 Velocity trigonometry of an SBVAWT blade

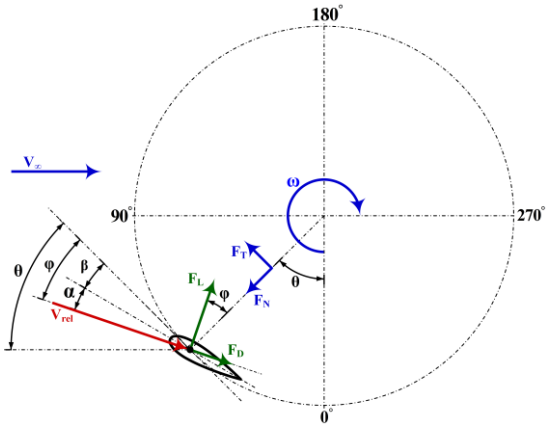

Fig. 3 Forces on an SBVAWT blade

Figure 2 shows the velocity trigonometry of a rotor blade in different areas, where ω denotes the angular velocity, V_t the tangential velocity, V_n the radial velocity, V_{rel} the relative velocity, θ the azimuth angle and φ the sum of the angle of attack and pitch angle, α is the angle of attack and β is the Pitch angle. The tangential and radial velocities are shown in Eq. (6) and (7) (Manatbayev et al., 2021). To numerically simulate the experimental model, the coordinate origin was placed on the bottom of the SBVAWT and the rotor was assumed to rotate in the clockwise (CW) direction. Here φ is the angle between the relative velocity vector and the tangent line to the circle given by Eq. (8). The angle of attack results from Eq. (9). It is the difference between φ and β (Yang et al., 2018).

$$V_t = V_{rel}\, cos\varphi = R\omega + V_\infty cos\theta \quad (\overrightarrow{R\omega}) \tag{6}$$

$$V_n = V_{rel}\, sin\varphi = V_\infty sin\theta \quad (\vec{R}) \tag{7}$$

$$\varphi = arctan\left(\frac{V_n}{V_t}\right) \tag{8}$$

$$\alpha = \varphi - \beta \tag{9}$$

Figure 3 shows the forces on an SBVAWT blade, where F_L and F_D represent the lift and drag forces, respectively. The lift and drag coefficients are given by Eq. (10) and (11) respectively (Maeda et al., 2015). Furthermore, F_T and F_N are the tangential forces given by Eq. (12) and (13) respectively (Yang et al., 2018). The magnitudes and directions of the lift, drag, tangential and radial forces depend on the blade position. The tangential and radial force coefficients are shown in Eq. (14) and (15) respectively (Maeda et al., 2015).

$$C_L = \frac{F_L}{\frac{1}{2}\rho c V_\infty^2} \tag{10}$$

$$C_D = \frac{F_D}{\frac{1}{2}\rho c V_\infty^2} \tag{11}$$

$$F_T = F_L sin\varphi - F_D cos\varphi \tag{12}$$

$$F_N = F_L cos\varphi - F_D sin\varphi \tag{13}$$

$$C_T = \frac{F_T}{\frac{1}{2}\rho c V_\infty^2} \tag{14}$$

$$C_N = \frac{F_N}{\frac{1}{2}\rho c V_\infty^2} \tag{15}$$

The moment coefficient of a rotor is the ratio of the rotor moment to the maximum moment as follows (Maeda et al., 2015):

$$C_m = \frac{M}{\frac{1}{2}\rho A R V_\infty^2} \tag{16}$$

Where A is the cross-sectional area of the rotor, which is defined as (Maeda et al., 2015, 2016):

$$A = 2R \times H \tag{17}$$

Rotor power is the ratio of rotor power production to maximum output power (Maeda et al., 2015, 2016):

$$C_P = \frac{P}{\frac{1}{2}\rho A V_\infty^3} \tag{18}$$

The tip speed ratio is obtained by dividing the tangential velocity by the wind speed (Maeda et al., 2017 Li et al., 2018a Guo et al., 2021a):

$$TSR = \frac{\omega R}{V_\infty} \tag{19}$$

2.3 Meshing

Figure 4 shows the control volume used to simulate the SBVAWT model. It consisted of fixed and rotating domains. The rotating domain includes the rotor, and the fixed domain surrounds the rotating domain. The domain was consistent with the experimental model of (Maeda et al., 2015). The same domain has been adopted in previous works on numerical simulation of SBVAWTs (Maeda et al., 2016 Baizhuma et al., 2021).

Figure. 5 shows the grid. Regular and irregular tetrahedral cells were applied to the fixed domain, while trihedral cells were used to mesh the rotating domain. In the fixed domain, finer meshes were used in areas closer to the rotating domain. In addition, a boundary layer grid was used around the rotor

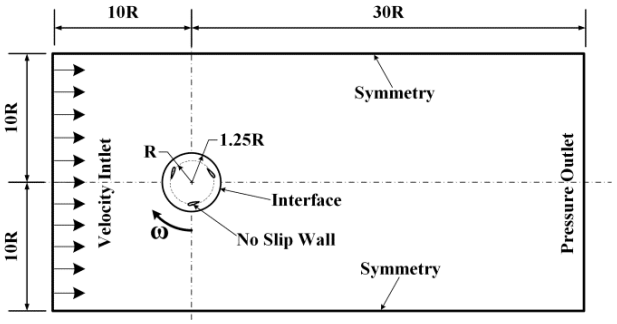

Fig. 4 2D SBVAWT domain and boundary conditions

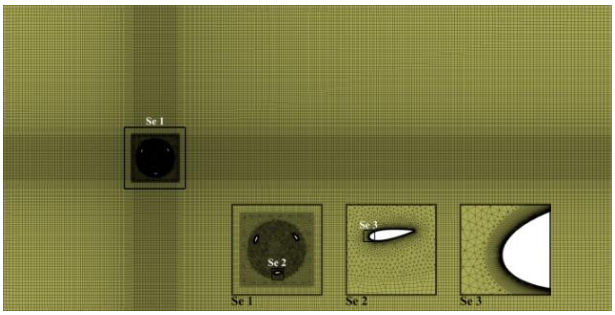

Fig. 5 Fixed and rotating 2D SBVAWT domains

Table 1 Meshed grid

First Cell Height Near Blade (mm)	0.01
y^+ Zone	0-0.95
Airfoil Edge Line Divisions	600
Number of Rotating Domain Cells	166,213
Number of Fixed Domain Cells	77,544
Total Number of Cells	243,834

blades to obtain accurate results. Table 1 gives the meshing scheme.

2.4 Simulation Settings

The present study assumed a single-phase and transient flow and neglected gravity. Air with a density of 1.225 kg/m3 and a dynamic viscosity of 1.7894×10-5 kg/m.s was used as the operating fluid. The rotation of the rotating domain in the fixed domain was modeled using the sliding mesh technique. The angular velocity of the rotor was set to 14.24 rad/s to obtain a tip speed ratio of 1.78. The input velocity was set to 8 m/s with 0.5% turbulence as input boundary conditions, and the output pressure was assumed to be equal to the ambient pressure with 0.5% turbulence as output boundary conditions. The rotor cross-sectional area was assumed to be 2.4 m^2. The termination criterion was 10^{-4} for the continuity equation, velocity in the x, y and z directions as well as the k and ω equations. The blade and rotor moments and powers were measured at each time step and the simulations were carried out on three rotors speed.

2.5 Grid Independence

To evaluate grid independence, seven grids with different mesh schemes were used. A total of 21,326—299,342 cells were applied as indicated in Table 2.

Table 2 Grid independence at a tip speed ratio of 1.78

Grid	y^+ Zone	Total Number of Cells	Difference between Grids
1	0-30	21,326	-
2	0-23.5	44,072	Variable
3	0-8.8	85,723	Variable
4	0-5.5	127,883	Variable
5	0-3.25	173,701	Variable
6	0-0.95	243,834	Variable
7	0-0.95	299,342	Fixed

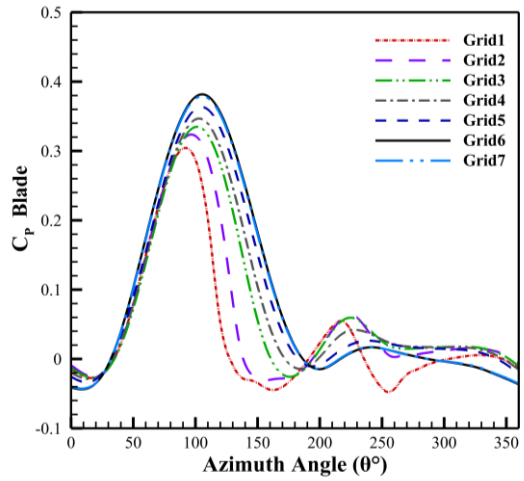

Fig. 6 Blade power coefficient at a tip speed ratio of 1.78

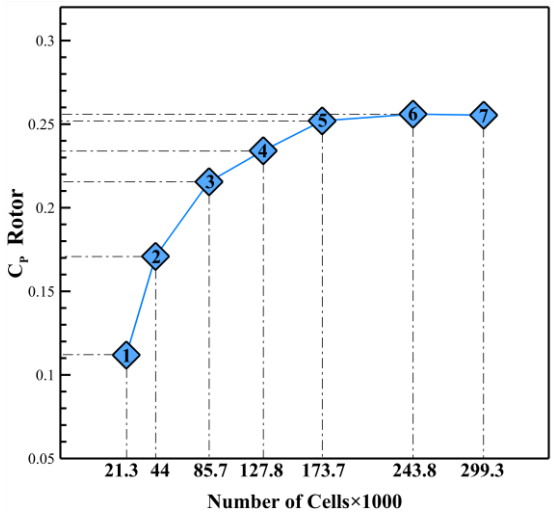

Fig. 7 Rotor power coefficient at a tip speed ratio of 1.78

Figure 6 and 7 show the blade power coefficient and the rotor power coefficient at a time step of 0.001 s (one degree of blade rotation). Increasing the number of cells significantly changed the blade power coefficient. The power coefficient increased at 0—180° and the power fluctuation decreased at 180—360° upon an increase in the number of cells. The rotor blade power coefficient changed with increasing cell number in grids 1—6 However, grids 6 and 7 showed almost the same

Table 3 Time steps at an angular velocity of 14.24 rad/s

Time Step (s)	0.006	0.001	0.0003	0.0001
Angle Travelled (°)	5	1	0.25	0.125

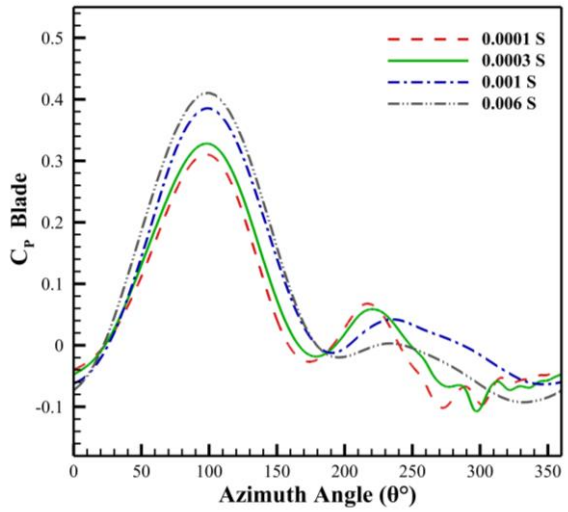

Fig. 8 Blade power coefficient at a tip speed ratio of 1.78 for different time steps

blade power coefficient. Increasing the cell number from 21,326 to 243,834 increased the average rotor power coefficient, while further increasing the cell number to 299,342 resulted in no significant change in the rotor average power coefficient. Therefore, grid 6 with 243,834 cells was used as the optimal grid for the simulations.

2.6 Time Step Independence

The time step independence was studied at an angular velocity of 14.24 rad/s and a wind speed of 8 m/s, as shown in Table 3. According to Fig. 8, reducing the time step from 0.006 to 0.001 s decreased the blade power coefficient at 0—180° and increased at 180—360°. The blade power coefficient apparently did not agree with the k-ω SST turbulence model (Maeda et al., 2017) at time steps of 0.001 and 0.006 s. Changing the time step to 0.0003 decreased the blade power coefficient at 0—180°, and the fluctuation of the power coefficient at 180—360° was more consistent with the k-ω turbulence model. In a time step of 0.0001 s, the blade power coefficient decreased at 0—180° and its fluctuation showed no significant change at 180—360°. Although the blade power coefficient changed slightly as the time step decreased from 0.0003 to 0.0001 s, the fluctuation of the blade power coefficient was consistent, especially at 180—360°. It was concluded that the optimal time step is 0.0003 s, which corresponds to a quarter of the blade rotation.

2.7 Validation

Figure 9 compares the numerical blade power coefficient with experimental data (Maeda et al., 2015)

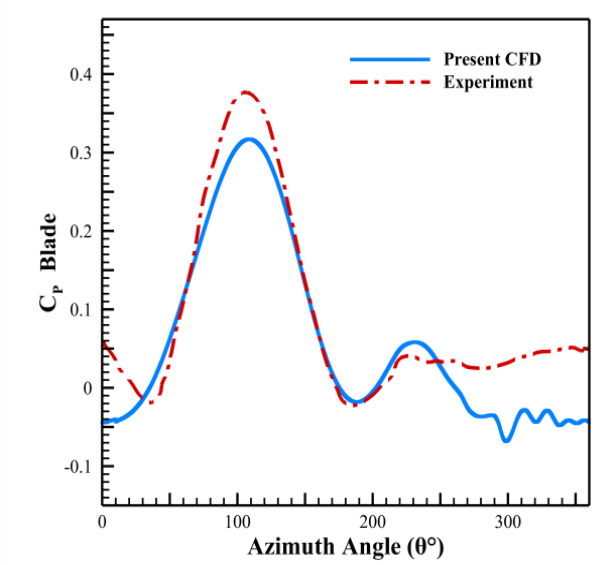

Fig. 9 Numerical versus experimental blade power coefficients at a tip speed ratio of 1.78 (Maeda et al., 2015)

at a tip speed ratio of 1.78. As can be seen, the numerical and experimental power coefficients were consistent despite the differences at 0—30°, 75—150°, and 250—360°. At 30—75° and 200—250°, the numerical method slightly overestimated the blade power coefficient. Furthermore, the numerical power coefficient had two peaks, while the experimental power coefficient only had a second peak. (Maeda et al., 2016) attributed the differences at the beginning and end of the path to the effects of peak vortex velocity on the flow, which could not be simulated in the 2D numerical model. They argued that the angle of attack was smaller than the stall angle, resulting in vortices at the blade tip that could not be simulation numerically. The difference in the middle of the path was attributed to the reduced flow force in part of the rotation path and the formation of resistance in the system. Due to the continuous change of the angle of attack in SBVAWTs and the flow separation over the blades, it is complex to accurately estimate this phenomenon using turbulence models, especially when the numerical model is two-dimensional while the real conditions are three-dimensional.

Figure 10 compares the numerical rotor power coefficient with experimental data (Maeda et al., 2015). As can be seen, the numerical and experimental rotor power coefficients were consistent at tip speed ratios up to 1.78 As the tip speed ratio increased above 1.78, the experimental power coefficient decreased while the numerical rotor power coefficient continued to increase. Li et al. (2018a) reported that the power was partially lost due to the mechanical power transmission system and the bearing and coupling elasticity, which are not included in the numerical model. They argued that vortices induce an opposing force that cannot be effectively simulated in 2D numerical models. (Howell et al., 2010) attributed this difference to the ineffectiveness of 2D numerical models in simulating blade tip vortices.

Table 4 Experimental and numerical ice formation parameters

Ref.	(Li et al., 2018a)	(Baizhuma et al., 2021)	
Simulation Model	EXP	CFD	CFD
Number of Blades	2 and 3	2	2
Rotor Diameter (mm)	440	440	170
Blade Height(mm)	250	2D	2D
Airfoil Profile	NACA 0018	NACA 0018	NACA 0015
Airfoil Chord Line Length (mm)	125	125	225
Wind Speed (m/s)	4	4	7
Tip Speed Ratio	0.2-1	1	2.29
Ambient Temperature (°C)	-6	-8	-8
Liquid Water Content (gr/m^3)	1.16	2.32	1
Median Volume Droplet Diameter (μm)	40	40	20
Icing Time (min)	5-30	30	30

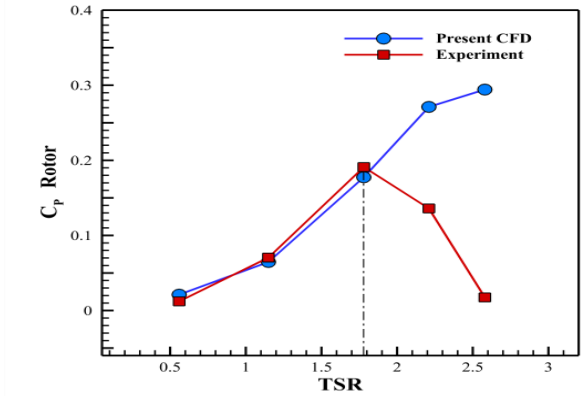

Fig. 10 Numerical versus experimental average rotor power coefficients (Maeda et al., 2015)

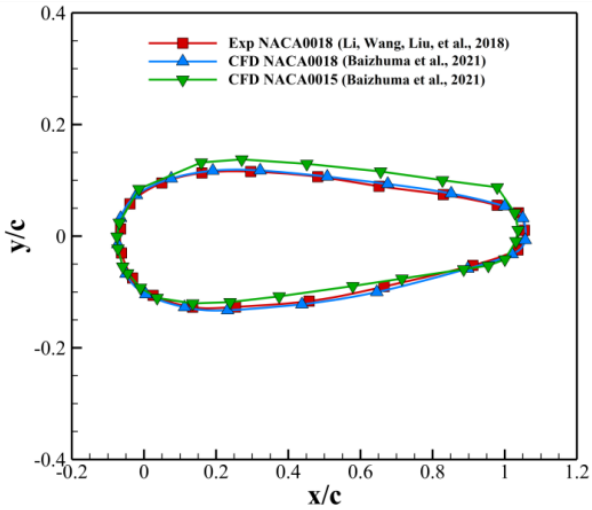

Fig. 11 Experimental versus numerical ice models

In the numerical simulation, the turbine power was partially lost through the arms, which is not taken into account in most numerical models. Furthermore, (Maeda et al., 2017) attributed these differences to the power consumption due to friction and vibration arising from the elasticity of components, which are not included in numerical models.

Examination of the conducted research allows us to conclude that the main reasons for the difference between the numerical and experimental simulation results are due to the type of two-dimensional flow analysis. In two-dimensional numerical simulation, velocity vectors in the X and Y directions are considered, but the velocity field in the Z direction is not considered. Therefore, the software is unable to model the vortices correctly, resulting in different numerical and experimental simulation results. In addition, the two-dimensional numerical simulation does not take into account things such as the inertia of the rotor blades, the effects of the arms and the central axis of the rotor on the flow, which affect the different results.

3. NUMERICAL SIMULATION OF AN ICED ROTOR

3.1 Ice Modelling

Li et al. (2018a) experimentally simulated ice on an SBVAWT, as shown in Table 4. They showed that an increase in the icing time and liquid water content increased the ice. It was found that the glaze ice thickness on the blade was not uniform with increasing the tip speed ratio. Figure 11 shows the experimental ice profile for a three-blade rotor with a liquid water content of 2.32 g/m^3, an icing time of 30 minutes, and a tip speed ratio of 1.

Baizhuma et al. (2021) numerically simulated the experimental model of (Li et al., 2018a) in ANSYS FENSAP-ICE (Table 4). According to Fig. 11, the numerical and experimental ice models agreed. (Baizhuma et al., 2021) numerically simulated ice on a different rotor with a different airfoil profile, rotor diameter and airfoil chord line length. As shown in Fig. 11, changing the airfoil profile, blade chord line length and rotor diameter from NACA 0018 to NACA 0015, 125 to 225 mm and 440 to 170 mm, respectively, had no significant influence on the ice shape and thickness. (Li et al., 2018a) reported an experimental ice simulation, in contrast, (Baizhuma et al., 2021) not only conducted numerical ice simulations but also studied the effects of ice formation on the performance of two-blade rotors. The aim of the present study was to evaluate in detail the effects of ice on the flow field around the rotor blades and the performance of a three-blade rotor.

The liquid water content, temperature, mean droplet diameter, icing time, wind speed and tip speed ratio were assumed to be 2.32 gr/m^3, -6 °C, 40 µm, 30 min, 4 m/s, and 1, respectively. However, the rotor diameter, airfoil profile and airfoil chord line length were 2000 mm, NACA 0021 and 265 mm, respectively.

A change airfoil surface is the ratio of the ice surface to the airfoil surface. the airfoil from NACA 0018 to NACA 0021, the wing area was increased However, the chord line was still not curved. As with NACA 0018, the NACA 0021 airfoil is symmetrical and no vortex would be created by the change in curvature of the airfoil. Vortices are the main factor in uneven ice distribution. Therefore, a non-curved profile chord line would result in an even distribution of ice. As a result, the rise in ice due to the increased airfoil area upon the change from NACA 0018 to NACA 0021 would be uniform. Furthermore, increasing the airfoil chord line length from 125 to 265 mm increased the ice cross section in proportion to the change in the airfoil profile area. Therefore, an increase in the airfoil area due to the changed profile and the length of the airfoil chord would increase the ice cross section if the airfoil is symmetrical and has a non-curved airfoil chord.

In SBVAWTs, vortices generated by blades with an angle of 0—180° flow toward the blades with an angle of 180—360°. You can influence the ice formation position on the blades in the range of 180-360°. The direction, velocity and size of the vortices depend on the wind speed, the angular velocity and the rotor diameter. Therefore, the only significant difference between the present work and (Li et al., 2018a) that affected ice shape and size was the rotor diameter (440 versus 2000 mm). However, a larger rotor diameter increases the length of the chord line in an SBVAWT, and the shape and path of the vortices are almost the same in SBVAWT. Therefore, in the present work, the experimental ice profile reported by (Li et al., 2018a) under the same aspect ratio was adopted to simulate the iced rotor.

3.2 Meshing and Numerical Settings of the Iced Rotor

To compare the iced and clean rotors, the geometric parameters of the clean rotor were used. The experimental ice profile reported by (Li et al., 2018a) was applied to the ice-free rotor under the same aspect ratio. Table 5 gives the grid parameters of the iced rotor. Figure 12 shows the meshed ice rotor model.

The governing equations of flow included the continuity and momentum equations. The flow was set as single-phase, incompressible and transient and the k-ω turbulence model was used. The rotating domain was assumed to rotate within the fixed domain using the slip mesh technique. Air with a density of 1.225 kg/m3 and a dynamic viscosity of 1.7894×10-5 kg/m.s was used as the operating fluid. The input boundary conditions included an input velocity of 8 m/s with a turbulence of 0.5%, while the output pressure was assumed to be equal to the ambient pressure with a turbulence of 0.5%. To compare the iced and clean rotors, the angular velocity was set to 14.24 rad/s.

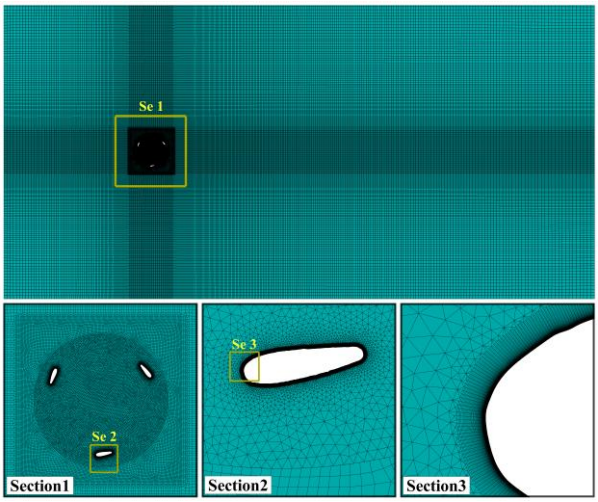

Fig. 12 2D meshed fixed and rotating domains of the iced SBVAWT

Table 5 Grid parameters of the iced SBVAWT

First Cell Height Near Blade (mm)	0.01
y^+ Zone	0-1
Airfoil Edge Line Divisions	730
Total Number of Rotating Domain Cells	195,299
Total Number of Fixed Domain Cells	77,030
Total Number of Cells	272,329

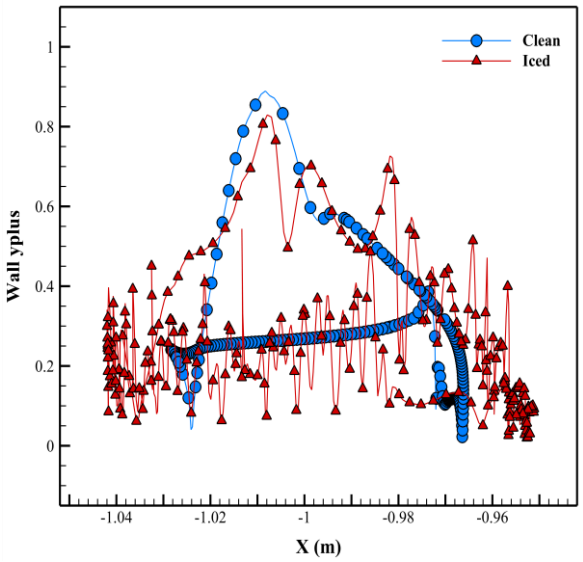

Fig. 13 y^+ on the ice-free and iced blades at 90°

Figure 13 shows the y+ diagrams at 90° angles on the surfaces of clean and iced blades. A boundary layer grid was installed in the wall area. Therefore, y+ was determined to be less than 1 for the iced and ice-free blades at a tip speed ratio of 1.78 for different angles. At this tip speed ratio, y+ was maximized at 90° for the clean blade. The meshing parameters of the clean rotor model were applied to the iced rotor. Likewise, y+ was maximized at 90° for the icy rotor and is subject to strong fluctuations on the suction and pressure surfaces.

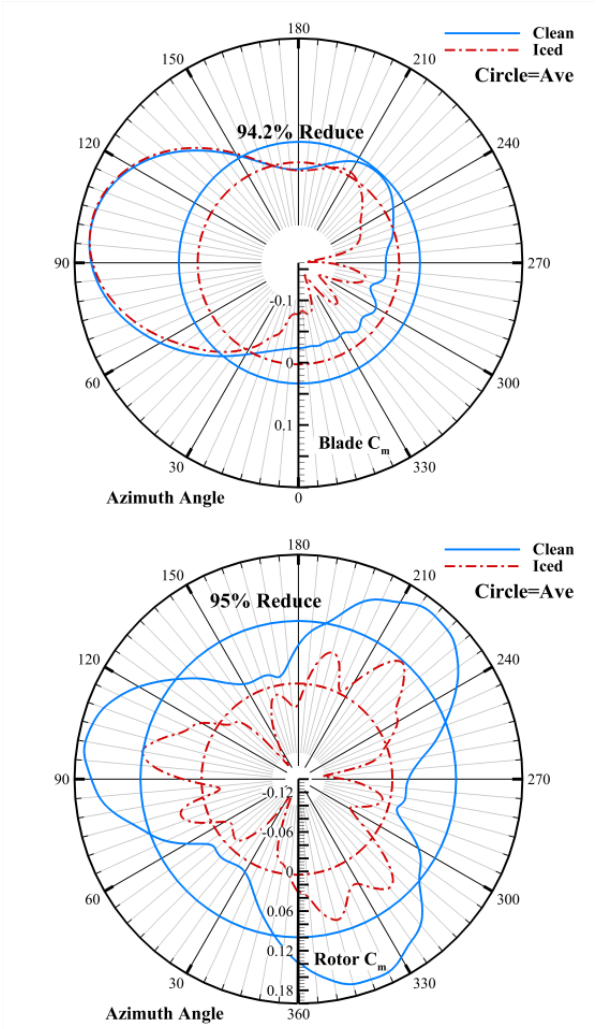

Fig. 14 Power coefficients of the ice-free versus iced blades at a tip speed ratio of 1.78

4. RESULTS AND DISCUSSION

Figure 14 shows the power coefficients of the ice-free and iced blades and rotors at a tip speed ratio of 1.78. Blade power was maximized at 30-150°. Due to the uneven, weakened wind flow, blade power was near zero or hostile at 180—360°. Ice formation resulted in a greater reduction in blade power at 180—360° than at 0—180°. The ice-free blade produced no energy at 160—190° and 25—250°. The maximum power coefficient of both ice-free and iced blades was 0.3 and occurred at 100°. The minimum power coefficient of the ice-free rotor blade was -0.07 and was 287°. Ice formation on the blade reduced the power coefficient to 30—180°. At 225—360°, the power coefficient not only decreased but also fluctuated greatly. The reduced power coefficient of the rotor blade reduced the power coefficient of the rotor over the rotation path. The reduction in the rotor's coefficient of performance was due to the changes in the velocity and pressure fields around the rotor blades, resulting in a decrease in performance. The blade performance coefficient remained almost unchanged at 30—180° when ice formed on the blade however, it decreased and fluctuated between 30 and 180°. At 25-250°, the power coefficient of the ice-free blade was slightly below zero When ice formed, it fell below zero at 30—150°, sometimes even reaching -0.27. The negative force is caused by the force on the blade in the opposite direction to the direction of rotation of the rotor. The ice formation on the rotor blades reduced the rotor's power coefficient throughout the rotation. The power coefficient of the iced rotor was positive, while that of the iced rotor fluctuated between negative and positive values. However, the power coefficient of the iced rotor was lower than that of the ice-free one throughout the entire rotation. Increasing the angle of attack resulted in flow separation behind the blades A larger angle of attack contributed to the vortex flow behind the rotor blades at angles of 180—360°. Due to the vortices that form behind the blades at 0—180° and their collisions with the blades at 180—360°, most of the power reduction of the blades occurs at 180—360°. Ice formation on the rotor blades contributes to vortex formation, which further degrades the performance of the rotor blades and rotor. Therefore, the blade power coefficients were reduced from 0.06 to 0.003 and the rotor power coefficient was reduced from 0.177 to 0.008 when ice formed. Ice formation resulted in an average reduction of 94.2% in blade power coefficient and 95% in rotor power coefficient.

Figure 15 shows the moment coefficients of the ice-free and iced rotor blades at a tip speed ratio of 1.78. The blade moment coefficient remained almost unchanged at 45—135° during ice formation. The moment coefficient of the icy rotor blades was almost the same as that of the ice-free blades up to 180°. At larger angles, ice formation reduced the moment coefficient. The ice formation not only reduced the moment coefficient but also caused a large variation of the moment coefficient at 225—315° and 315—45°. The minimum and maximum reduction of the ice-induced moment coefficient occurred at 45—315° and 225—315°respectively.

Figure 16 shows the average moment and power coefficients of the ice-free and iced blades at different angles for a tip speed ratio of 1.78. The maximum average moment and power of the ice-free blades occurred at 45—135°, while the average moment and power were minimized at 225—315°. On the other hand, the average moment and power of the iced rotor blades were maximized at 45—135° and minimized at 225—315°. The minimum and maximum reductions in average blade power and moment during ice formation were observed at 45—315° and 225—315°, respectively. Therefore, ice formation due to the SBVAWT structure resulted in a greater power reduction downstream.

Figure 17 shows the horizontal velocity component contours around the ice-free and iced blades at 225—360°. At 225°, a narrow region with significant horizontal velocity appeared between the leading edge and the trailing edge near the blade wall. Ice formation reduced the pressure behind the blade and increased the horizontal velocity component near the blade wall. Ice increased the windward surface of the blade and reduced the horizontal velocity component at the front and back of the blade. Therefore, the horizontal velocity component increased near the edge behind the blade and decreased at greater

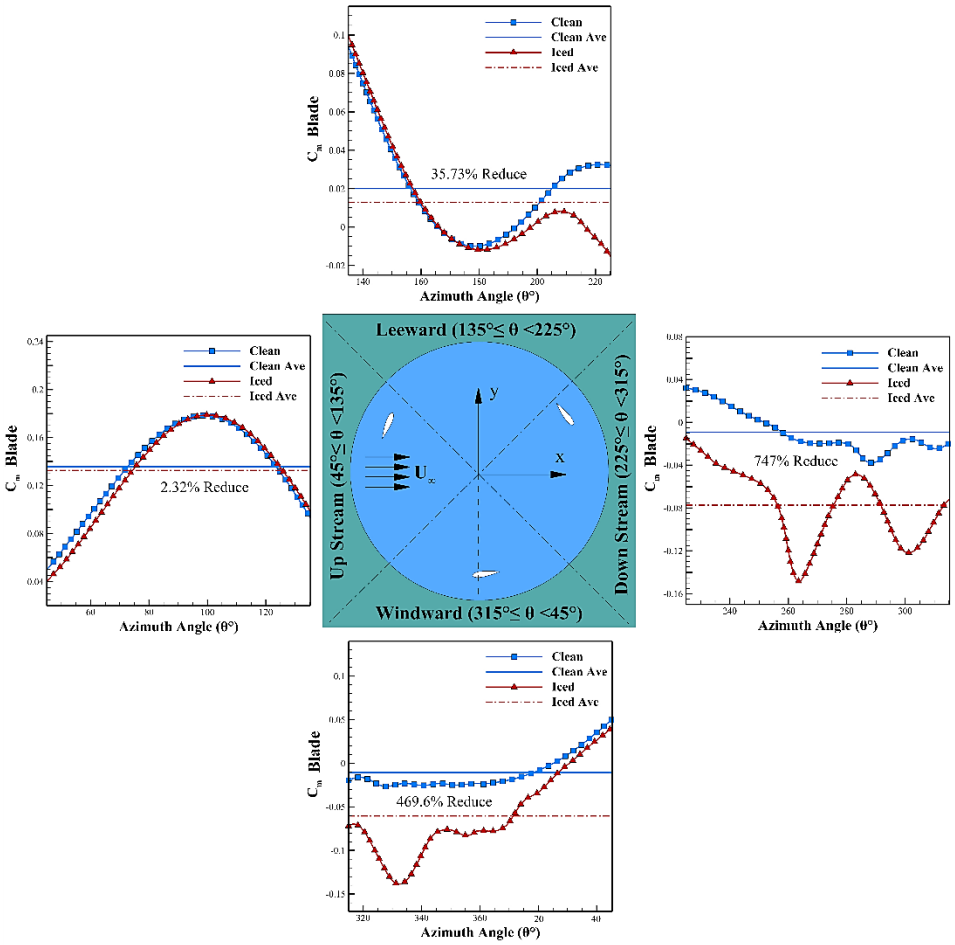

Fig. 15 Moment coefficients of the ice-free versus iced blades at a tip speed ratio of 1.78

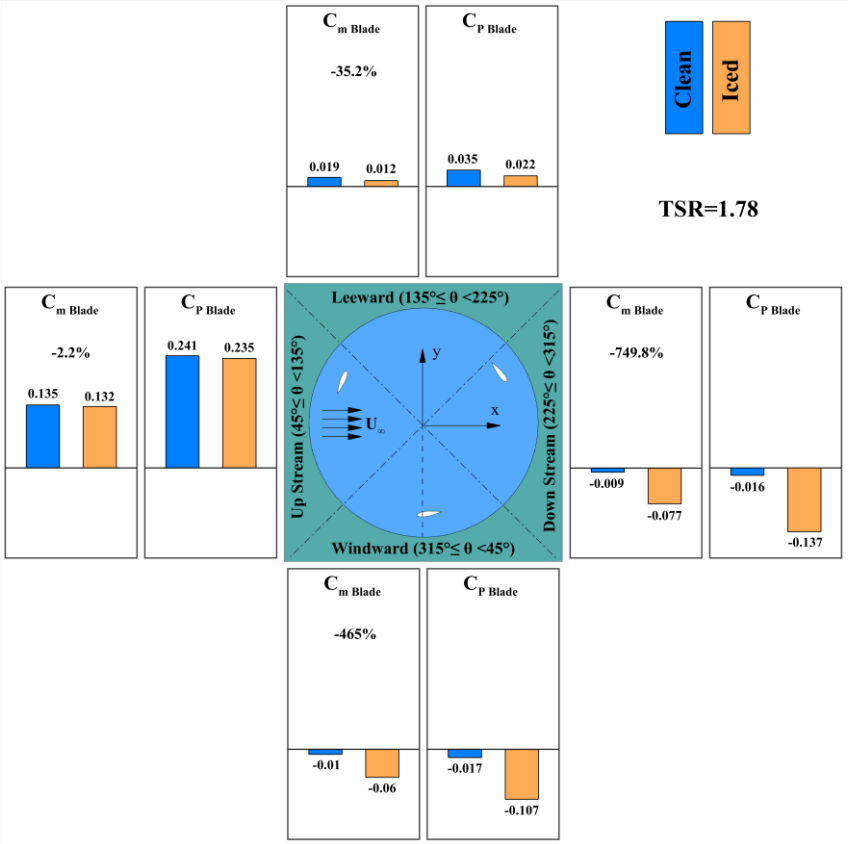

Fig. 16 Average blade power and moment coefficients at a tip speed ratio of 1.78

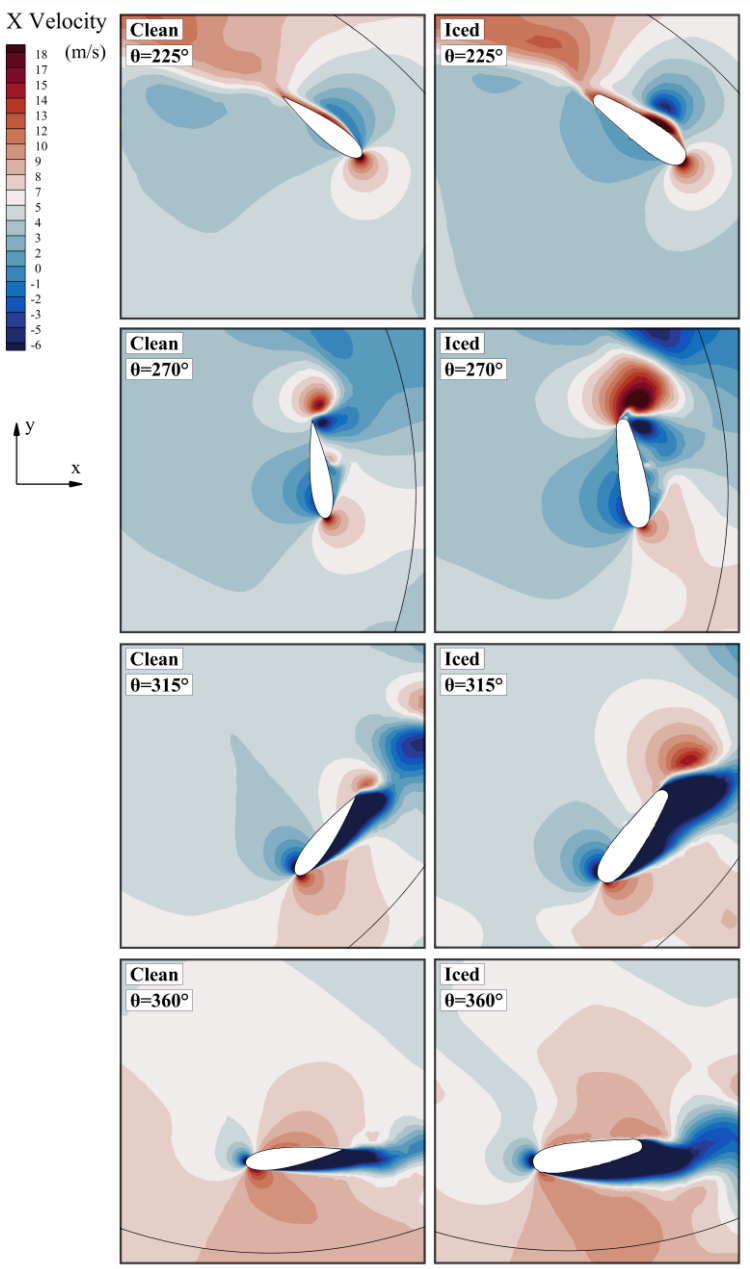

Fig. 17 Horizontal velocity component contours of the ice-free versus iced blades at a tip speed ratio of 1.78

distances behind the blade when ice formed. The mixture of two region with different horizontal velocity components changed the streamlines, increased the vortex magnitude, and reduced the tangential force and blade power. At 270°, ice increased the horizontal velocity component near the trailing edge. This high-velocity regime reduced the pressure near the trailing edge and changed the balance of forces between the trailing and leading edges. The reduced pressure and increased trailing edge velocity reduced blade power and performance. Ice formation at 280° reduced the horizontal velocity component in another area near the trailing edge. Therefore, the velocity difference between the high-velocity and low-velocity regimes near the trailing edge increased the vortex strength. The vortices increased flow turbulence near the trailing edge and reduced blade power. At 270°, ice formation reduced the horizontal velocity component at the front and rear of the blade and increased the velocity at the leading edge.

At 315°, an area with a small horizontal velocity component appeared on the back of the blade. Ice formation increased this low-velocity area and increased the horizontal velocity component near the trailing edge. The change in velocity in these region and the difference in velocity at their boundaries changed the flow field around the blade, particularly near the trailing edge. Therefore, it can be concluded that the power reduction of the rotor blade at 315° is due to flow field fluctuations behind the rotor blade near the trailing edge. For the ice-free blade, two low-velocity regions occurred near the trailing edge and the outer edge at 360°. Ice formation enlarged these low-velocity areas. In addition, ice increased the horizontal velocity component in the inner and outer regions. Thus, the reduction in the coefficient of power at 360° is due to the change in the flow field around

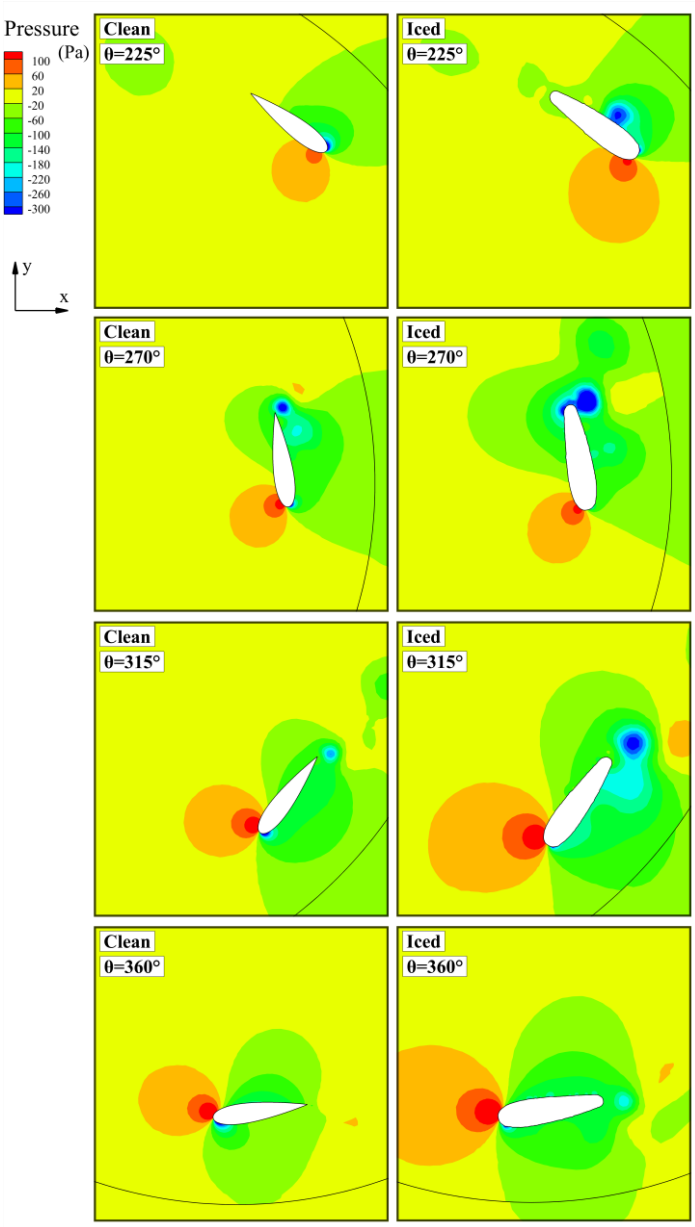

Fig. 18 Pressure contours around the ice-free versus iced blades at a tip speed ratio of 1.78

the blade and the increase in the vorticity force in the outer regions of the blade.

Figure 18 shows the pressure contours around the ice-free and iced blades at 225-360°. Ice formation increased the high pressure area near the leading edge at 225°, resulting in a low pressure area near the outer edge. In general, frost reduced the pressure behind the blade at 225°. The reduced pressure behind the blade and the low pressure regime near the outer edge during ice formation resulted in vortex formation. The vortices and pressure changes at the inner and outer edges of the blade changed the flow field around the blade and reduced blade power at 225°. Ice formation on the rotor blades at 270° increased the high pressure area near the leading edge and the low pressure area near the trailing edge. In addition, ice enlarged the low pressure zone on the inner edge. Therefore, the pressure changes around the blade as ice formed changed the forces acting on the blade and reduced blade power. The area of high pressure near the leading edge rose 315°, with an area of low pressure forming near the trailing edge. These two regimes reduced blade power at 315°. At 360°, the high pressure area near the leading edge increased, creating a counterforce and reducing blade power. Therefore, ice changed the pressure field around the blade and reduced blade power, especially at 225°, 270°, 315° and 360°.

Figure 19 shows the streamlines near ice-free and iced rotor blades at 215-360°. There was a small vortex near the outer edge of the ice-free blade at 225° that increased as ice formed. At the center of the vortex the pressure was reduced and the velocity was low. At 270°, a small vortex appeared some distance from the trailing edge, which disappeared as ice formed, with a stronger vortex forming near the trailing edge. The low pressure at the center of this vortex exerted a counterforce on the blade. At a certain distance from the trailing edge at 315°, a vortex formed, which increased in size and flowed into the area behind the blade when ice formed.

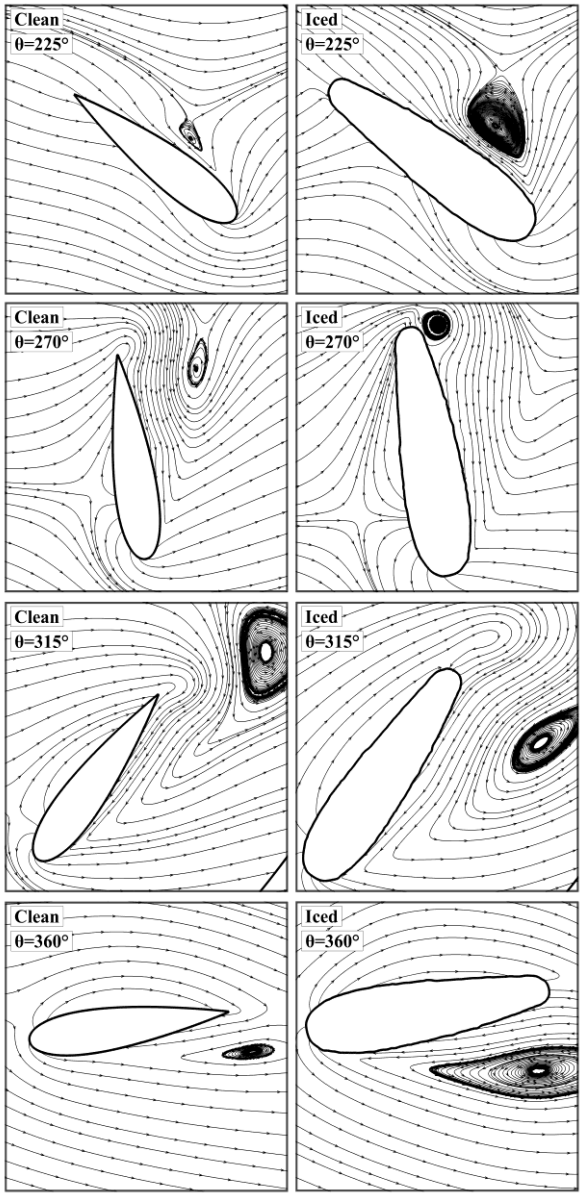

Fig. 19 Streamlines downstream of the ice-free versus iced blades at a tip speed ratio of 1.78

There was a vortex near the trailing edge at 360°, and the ice increased the vortex dramatically. Therefore, ice formation increased vortex strength and moved the vortices closer to the blade at some angles and to other areas at other angles. This changed the pressure and velocity fields around the blade, reducing blade power.

Figure 20 shows the turbulence contours in the clean and icy rotating area. Ice formation increased turbulence near the blade wall, particularly in the tail area near the trailing edge. Therefore, the flow field around the blades changed, resulting in lower output power. The rotor blades were exposed to turbulence and vortices at 180—360°, which were induced at 0—180°. These vortices changed the flow around the blades and reduced blade power. Therefore, increasing the number of SBVAWT blades would reduce performance. At 105° and 120° turbulent flow occurred in the ends of the blades. It collided with the rotor blades at 0° and 345°.

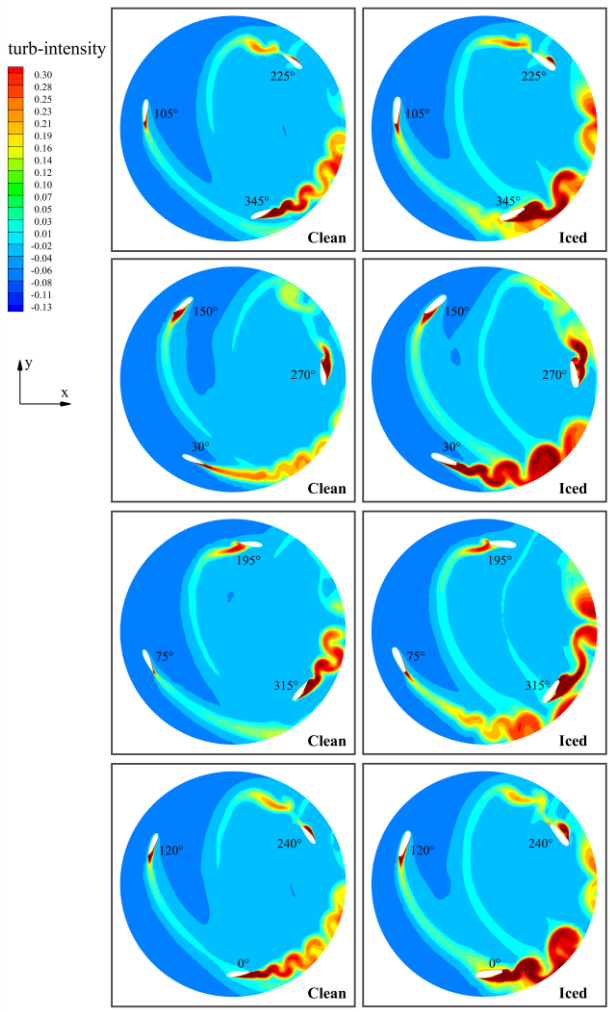

Fig. 20 Turbulence contours around the ice-free versus iced rotors at a tip speed ratio of 1.78

Therefore, there was a power reduction for the rotor blades at 0° and 315°.

5. CONCLUSIONS

In this work, a three-blade SBVAWT was numerically simulated in two dimensions to evaluate the effects of ice formation on the blades in time-dependent environments. The results can be summarized as follows.

1) Ice formation reduced blade power and increased its fluctuations at 180-360°, resulting in a 94.2% reduction in the average blade power coefficient.

2) Ice formation reduced the rotor power and increased its fluctuations throughout the rotation path, resulting in a 95% reduction in the average rotor power coefficient.

3) Ice formation changed the velocity field around the blades and reduced blade power at 180-360°.

4) Ice formation increased the pressure on the leading edge by 180—360° and decreased the pressure near the trailing edge at some angles. The changes in the pressure field reduced the performance of the rotor blades.

5) Ice formation increased vorticity strength. It moved the vortices closer to the blade at some angles and to other areas at other angles. This changed the velocity and pressure fields around the rotor blades and reduced the rotor blade power.

6) Ice formation increased turbulence near the rotor blades, particularly in the tail near the trailing edge. Due to the increased turbulence, the rotor blades generated vortices at 0-180°. The vortices flowed and collided with the rotor blades at an angle of 180—360°. Therefore, the blades at 180-360° produced significantly lower power than those at 0-180°.

6. FURTHER PLANS AND FUTURE WORKS

This work investigates the effects of ice formation on a three-blade wind turbine with straight vertical-axis blades. Due to the reduction of calculation errors and the application of more realistic conditions, the effects of ice can now be analyzed in future work in three-dimensional numerical simulations, experimental simulations and two-phase flow simulation. It is also possible to simulate the effects of ice on two, four, five and six blade rotors.

CONFLICT OF INTERESTS

The authors have no conflicts to disclose.

AUTHORS CONTRIBUTIONS

Sarallah Abbasi: Writing – original draft, review & editing, Supervision, Resources, Investigation, Project administration, Methodology, Investigation, Data curation, Conceptualization; **Ali Mahmoodi**: Writing – original draft, Visualization, Validation, Software, Resources, Methodology, Investigation, Formal analysis, Data curation, Conceptualization; **Ali Joodaki:** Writing – review & editing, Writing – original draft, Conceptualization, Resources, Formal analysis.

REFERENCES

Baizhuma, Z., Kim, T., & Son, C. (2021). Numerical method to predict ice accretion shapes and performance penalties for rotating vertical axis wind turbines under icing conditions. *Journal of Wind Engineering and Industrial Aerodynamics*, *216*, 104708. https://doi.org/10.1016/j.jweia.2021.104708

Ebrahimi, A., Hajipour, M., & Hasheminasab, H. (2016). Experimental investigation on the aerodynamic performance of NLF-0414 iced-airfoil. Journal of Applied Fluid Mechanics, 9(2), 587-592. https://doi.org/10.18869/acadpub.jafm.68.225.24606

Gao, L., & Hong, J. (2021). Wind turbine performance in natural icing environments: A field characterization. *Cold Regions Science and Technology*, *181*, 103193. https://doi.org/10.1016/j.coldregions.2020.103193

Gao, L., & Hu, H. (2021). Wind turbine icing characteristics and icing-induced power losses to utility-scale wind turbines. *Proceedings of the National Academy of Sciences*, *118*(42), e2111461118. https://doi.org/10.1073/pnas.2111461118

Gao, L., Tao, T., Liu, Y., & Hu, H. (2021). A field study of ice accretion and its effects on the power production of utility-scale wind turbines. *Renewable Energy*, *167*, 917-928. https://doi.org/10.1016/j.renene.2020.12.014

Guo, W., Shen, H., Li, Y., Feng, F., & Tagawa, K. (2021a). Wind tunnel tests of the rime icing characteristics of a straight-bladed vertical axis wind turbine. *Renewable Energy*, *179*, 116-132. https://doi.org/10.1016/j.renene.2021.07.033

Guo, W., Zhang, Y., Li, Y., Tagawa, K., & Zhao, B. (2021b). A Wind Tunnel Experimental Study on the Icing Characteristics of a Cylinder Rotating around a Vertical Axis. *Applied Sciences*, *11*(21), 10383. https://doi.org/10.3390/app112110383

Howell, R., Qin, N., Edwards, J., & Durrani, N. (2010). Wind tunnel and numerical study of a small vertical axis wind turbine. *Renewable Energy*, *35*(2), 412-422. https://doi.org/10.1016/j.renene.2009.07.025

Hu, L., Zhu, X., Chen, J., Shen, X., & Du, Z. (2018). Numerical simulation of rime ice on NREL Phase VI blade. *Journal of Wind Engineering and Industrial Aerodynamics*, *178*, 57-68. https://doi.org/10.1016/j.jweia.2018.05.007

Hu, L., Zhu, X., Hu, C., Chen, J., & Du, Z. (2017). Wind turbines ice distribution and load response under icing conditions. *Renewable Energy*, *113*, 608-619. https://doi.org/10.1016/j.renene.2017.05.059

Ibrahim, G., Pope, K., & Muzychka, Y. (2018). Effects of blade design on ice accretion for horizontal axis wind turbines. *Journal of Wind Engineering and Industrial Aerodynamics*, *173*, 39-52. https://doi.org/10.1016/j.jweia.2017.11.024

Imran, R. M., Hussain, D. A., & Soltani, M. (2016). An experimental analysis of the effect of icing on Wind turbine rotor blades. 2016 IEEE/PES Transmission and Distribution Conference and Exposition (T&D), https://doi.org /10.1109/TDC.2016.7520041

Jin, J. Y., & Virk, M. S. (2020a). Effect of Wind Turbine Blade Profile Surface Roughness on Ice Accretion–A Numerical Case Study. IOP Conference Series: Earth and Environmental Science, https://doi.org /10.1088/1755-1315/603/1/012045

Jin, J. Y., & Virk, M. S. (2020b). Experimental study of ice accretion on S826 & S832 wind turbine blade profiles. *Cold Regions Science and Technology*, *169*, 102913. https://doi.org/10.1016/j.coldregions.2019.102913

Kreutz, M., Ait-Alla, A., Varasteh, K., Oelker, S., Greulich, A., Freitag, M., & Thoben, K.-D. (2019). Machine learning-based icing prediction on wind turbines. *Procedia Cirp*, *81*, 423-428. https://doi.org/10.1016/j.procir.2019.03.073

Lamraoui, F., Fortin, G., Benoit, R., Perron, J., & Masson, C. (2014). Atmospheric icing impact on wind turbine production. *Cold Regions Science and Technology*, *100*, 36-49. https://doi.org/10.1016/j.coldregions.2013.12.008

Li, Y., Shi, L., Guo, W., Sun, C., & Jiang, Y. (2020). Wind Tunnel Test of the Icing Characteristics of Airfoil Rotating around a Vertical Axis. *International Journal of Rotating Machinery*, *2020*, 1-17. https://doi.org/10.1155/2020/8841076

Li, Y., Sun, C., Jiang, Y., & Feng, F. (2019a). Scaling method of the rotating blade of a wind turbine for a rime ice wind tunnel test. *Energies*, *12*(4), 627. https://doi.org/10.3390/en12040627

Li, Y., Sun, C., Jiang, Y., Yi, X., & Zhang, Y. (2019b). Effect of liquid water content on blade icing shape of horizontal axis wind turbine by numerical simulation. *Thermal Science*, *23*(3 Part A), 1637-1645. https://doi.org/10.2298/TSCI180627234L

Li, Y., Tagawa, K., & Liu, W. (2010). Performance effects of attachment on blade on a straight-bladed vertical axis wind turbine. *Current Applied Physics*, *10*(2), S335-S338. https://doi.org/10.1016/j.cap.2009.11.072

Li, Y., Tagawa, K., Feng, F., Li, Q., & He, Q. (2014). A wind tunnel experimental study of icing on wind turbine blade airfoil. *Energy Conversion and Management*, *85*, 591-595. https://doi.org/10.1016/j.enconman.2014.05.026

Li, Y., Tang, J., Liu, Q., Wang, S., & Feng, F. (2015). A visualization experimental study of icing on blade for VAWT by wind tunnel test. 2015 International conference on power electronics and energy engineering, https://doi.org /10.2991/peee-15.2015.39

Li, Y., Wang, S., Liu, Q., Feng, F., & Tagawa, K. (2018a). Characteristics of ice accretions on blade of the straight-bladed vertical axis wind turbine rotating at low tip speed ratio. *Cold Regions Science and Technology*, *145*, 1-13. https://doi.org/10.1016/j.coldregions.2017.09.001

Li, Y., Wang, S., Sun, C., Yi, X., Guo, W., Zhou, Z., & Feng, F. (2018b). Icing distribution of rotating blade of horizontal axis wind turbine based on Quasi-3D numerical simulation. *Thermal Science*, *22* (Suppl. 2), 681-691. https://doi.org /10.2298/TSCI170821053L

Maeda, T., Kamada, Y., Hiromori, Y., Nakai, A., & Kasuya, T. (2017). Study on stall behavior of a straight-bladed vertical axis wind turbine with numerical and experimental investigations. *Journal of Wind Engineering and Industrial Aerodynamics*, *164*, 1-12. https://doi.org/10.1016/j.jweia.2017.02.005

Maeda, T., Kamada, Y., Murata, J., Furukawa, K., & Yamamoto, M. (2015). Effect of number of blades on aerodynamic forces on a straight-bladed Vertical Axis Wind Turbine. *Energy*, *90*, 784-795. https://doi.org/10.1016/j.energy.2015.07.115

Maeda, T., Kamada, Y., Murata, J., Kawabata, T., Shimizu, K., Ogasawara, T., Kasuya, T. (2016). Wind tunnel and numerical study of a straight-bladed vertical axis wind turbine in three-dimensional analysis (Part I: For predicting aerodynamic loads and performance). *Energy*, *106*, 443-452. https://doi.org/10.1016/j.energy.2016.03.089

Manatbayev, R., Baizhuma, Z., Bolegenova, S., & Georgiev, A. (2021). Numerical simulations on static Vertical Axis Wind Turbine blade icing. *Renewable Energy*, *170*, 997-1007. https://doi.org/10.1016/j.renene.2021.02.023

Sagol, E. (2014). *Three Dimensional Numerical Predicton of Icing Related Power and Energy Losses on a Wind Turbine* École Polytechnique de Montréal].https://publications.polymtl.ca/1476/

Shi, L., Li, Y., Guo, W., & Sun, C. (2021). Experimental Research on the Similarity of Rime Icing on a Cylinder Rotating around Its Horizontal Axis. *International Journal of Rotating Machinery*, *2021*, 1-14. https://doi.org/10.1155/2021/9986733

Shu, L., Li, H., Hu, Q., Jiang, X., Qiu, G., He, G., & Liu, Y. (2018a). 3D numerical simulation of aerodynamic performance of iced contaminated wind turbine rotors. *Cold Regions Science and Technology*, *148*, 50-62.https://doi.org/10.1016/j.coldregions.2018.01.008

Shu, L., Li, H., Hu, Q., Jiang, X., Qiu, G., McClure, G., & Yang, H. (2018b). Study of ice accretion feature and power characteristics of wind turbines at natural icing environment. *Cold Regions Science and Technology*, *147*, 45-54.https://doi.org/10.1016/j.coldregions.2018.01.006

Shu, L., Liang, J., Hu, Q., Jiang, X., Ren, X., & Qiu, G. (2017). Study on small wind turbine icing and its performance. *Cold Regions Science and Technology*, *134*, 11-19. https://doi.org/10.1016/j.coldregions.2016.11.004

Son, C., & Kim, T. (2020). Development of an icing simulation code for rotating wind turbines. *Journal of Wind Engineering and Industrial Aerodynamics*, *203*, 104239. https://doi.org/10.1016/j.jweia.2020.104239

Son, C., Kelly, M., & Kim, T. (2021). Boundary-layer transition model for icing simulations of rotating wind turbine blades. *Renewable Energy*, *167*, 172-183. https://doi.org/10.1016/j.renene.2020.11.070

Turkyilmazoglu, M. (2002a). Flow in the vicinity of the trailing edge of Joukowski-type profiles. Proceedings of the Royal Society of London. Series A: Mathematical, Physical and Engineering Sciences, 458(2023), 1653-1672.https://doi.org/10.1098/rspa.2001.0942

Turkyilmazoglu, M. (2002b). The absolute instability of Joukowski-type airfoils. Theoretical and computational fluid dynamics, 15(4), 255-264. https://doi.org/10.1007/s001620100053

Turkyilmazoglu, M., GajjarRID=" 1" ID=" 1" All correspondence should be addressed to Dr. JSB Gajjar, J. S. B., & Ruban, A. I. (1999). The absolute instability of thin wakes in an incompressible/compressible fluid. Theoretical and computational fluid dynamics, 13, 91-114.https://doi.org/10.1007/S001620050006

Wang, Q., Yi, X., Liu, Y., Ren, J., Li, W., Wang, Q., & Lai, Q. (2020). Simulation and analysis of wind turbine ice accretion under yaw condition via an Improved Multi-Shot Icing Computational Model. *Renewable Energy*, *162*, 1854-1873. https://doi.org/10.1016/j.renene.2020.09.107

Yang, Y., Guo, Z., Song, Q., Zhang, Y., & Li, Q. a. (2018). Effect of blade pitch angle on the aerodynamic characteristics of a straight-bladed vertical axis wind turbine based on experiments and simulations. *Energies*, *11*(6), 1514. https://doi.org/10.3390/en11061514

Yirtici, O., & Tuncer, I. H. (2021). Aerodynamic shape optimization of wind turbine blades for minimizing power production losses due to icing. *Cold Regions Science and Technology*, *185*, 103250. https://doi.org/10.1016/j.coldregions.2021.103250

Yirtici, O., Ozgen, S., & Tuncer, I. H. (2019). Predictions of ice formations on wind turbine blades and power production losses due to icing. *Wind Energy*, *22*(7), 945-958. https://doi.org/10.1002/we.2333

Zhu, C., Zhu, C., Guo, T., & Liu, L. (2015). Development and Validation of Aircraft Icing Computational Simulation Code. 2nd International Conference on Intelligent Computing and Cognitive Informatics (ICICCI 2015).https://doi.org /10.2991/icicci-15.2015.14

Zhu, X., Hu, L., Chen, J., Shen, X., & Du, Z. (2018). Calculation of Collection Efficiency on NREL Phase VI Blade. *Journal of Energy Resources Technology*, *140*(7), 071202. https://doi.org/10.1115/1.4039349